Assessments of Hollow Cathode Wear in the Xenon Ion Propulsion System (XIPS©) by Numerical Analyses and Wear Tests

Ioannis G. Mikellides,* Ira Katz,† Dan M. Goebel,‡ and James E. Polk§
Jet Propulsion Laboratory, California Institute of Technology, Pasadena, CA, 91109

The standard approach presently followed by NASA to qualify electric propulsion for the required mission throughput has been based largely on life tests, which can be costly and time consuming. Revised electric propulsion life-qualification approaches are being formulated that combine analytical and/or computational methods with (shorter-duration) wear tests. As a model case, a wear test is being performed at JPL to assess the lifetime of the discharge hollow cathode in the Xenon Ion Propulsion System (XIPS©), a 25-cm ion engine developed by L-3 Communications Electron Technologies, Inc. for commercial applications. Wear and plasma data accumulated throughout this life-assessment program are being used to validate the existing 2-D hollow cathode code OrCa2D. We find that the OrCa2D steady-state solution predicts very well the time-averaged plasma data and the keeper voltage after 5500 hrs of operation in high-power mode. When the wave motion that occurs naturally in these devices is accounted for, based on an estimate of the maximum wave amplitude, the molybdenum-keeper erosion profile observed in the XIPS© discharge cathode is also reproduced within a factor of two of the observation. When the same model is applied to predict the erosion of a tantalum keeper we find that erosion is reduced by more than two orders of magnitude compared to the molybdenum keeper due the significantly lower sputtering yield of tantalum. A tantalum keeper would therefore allow keeper lifetimes that greatly exceed the present requirements for deep-space robotic missions considered by NASA. Moreover, such large reduction of the erosion renders the largest uncertainties in the models, which are associated with the wave amplitude estimates and the electron transport model, negligible.

I. Nomenclature

A = amplitude factor of plasma oscillation
I_K = keeper current, A
$\mathbf{j}_e$ = electron current density, A/m^2
$j_{e,th}$ = electron thermal current density, A/m^2
$\mathbf{j}_i$ = ion current density, A/m^2
k_B = Boltzmann's constant, J/K
m_i = mass of xenon ion, kg
m_e = mass of electron, kg
$\hat{\mathbf{n}}$ = normal unit vector
n_e = electron number density, particles/m^3
u_e = electron drift speed, m/s
$u_{T,e}$ = electron thermal speed $(2k_BT_e/m_e)^{1/2}$, m/s
V_K = keeper voltage, V
Y = sputtering yield, atoms/ion
z = axial coordinate, m

Greek Symbols

α = anomalous collision frequency coefficient
ε_i = ion energy, J
η = plasma resistivity, Ohm-m

* Member Technical Staff, Electric Propulsion Group, 4800 Oak Grove Drive, Pasadena, CA, 91109, Mail Stop 125-109, Senior Member AIAA.
† Group Supervisor, Electric Propulsion Group, 4800 Oak Grove Drive, Pasadena, CA, 91109, Mail Stop 125-109, Senior Member AIAA.
‡ Section Staff, Thermal and Propulsion Engineering Section, 4800 Oak Grove Drive, Pasadena, CA, 91109, Mail Stop 125-109, Senior Member AIAA.
§ Section Staff, Thermal and Propulsion Engineering Section, 4800 Oak Grove Drive, Pasadena, CA, 91109, Mail Stop 125-109, Senior Member AIAA.

q_e = charge, 1.602×10^{-19} C
r = radial coordinate, m
S_K = keeper current-collection area, m^2
T_e = electron temperature, K
T_i = ion temperature, K
θ = angle associated with plasma oscillations, rad
ν_α = anomalous collision frequency, s^{-1}
ν_{ei} = electron-ion collision frequency, s^{-1}
ν_{en} = electron-neutral collision frequency, s^{-1}
ϕ = plasma potential, V
ω_{pe} = electron plasma frequency, rad/s

II. Introduction

THE first application of an ion engine on a NASA planetary mission was the Deep Space 1 (DS1) technology demonstration mission, which was launched about a decade ago. The engine was a 30-cm ion thruster that was developed by the NASA Glenn Research Center, with contributions from several other partners, under the NASA Solar Electric Propulsion (SEP) Technology Applications Readiness (NSTAR) program. The agency's second application is onboard the Dawn spacecraft, launched successfully onboard a Delta II rocket in September of 2007 for a mission to the two largest inhabitants of the asteroid belt: Vesta and Ceres. The spacecraft has three onboard ion engines that are based on the NSTAR (30-cm) technology. All three engines have successfully demonstrated operation onboard the spacecraft.

The Dawn mission encountered a number of delays and cost overruns before launch that were partly attributed to the first implementation of ion engine technology on a NASA science mission. In the commercial sector ion engine development evolved differently, largely due to the less demanding mission requirements associated with commercial thruster applications. For example, in 1999 Boeing launched the first 702 communications satellite that employed four 25-cm Xenon Ion Propulsion Systems (XIPS© Fig. 1), and since then over 50 additional such thrusters have been flown with no thruster failures. To support the ongoing commercial demand a XIPS© product line is currently in place, which sustains the expertise associated with the manufacturing of these thrusters. Commercial Hall thrusters are also available in the U.S. from Space Systems Loral, Aerojet and Busek. This availability of commercial EP offers the potential for significant cost reductions on many science missions considered by NASA; by buying "off the assembly line" of existing product lines the cost associated with the infrequent development of thruster components for science missions may be significantly reduced.[1,2]

Fig. 1. The 25-cm Xenon Ion Propulsion System (XIPS©) is produced by L-3 Communications Electron Technologies, Inc.

For commercial applications, the 25-cm XIPS© is designed to operate in two modes: the high-power (HP) mode (4.5 kW), delivering 3500 seconds of specific impulse and 166 mN of thrust, and the low-power (LP) mode (2.3 kW) with a specific impulse of 3400 seconds and thrust of 80 mN. A detailed performance comparison between the 25-cm XIPS and the NSTAR 30-cm ion engine is provided in Ref. 3. The lifetime requirement for such applications is 1000 hrs in HP mode and almost 11,000 hrs in LP mode. In general, NASA science missions have more demanding life and throttling requirements for the electric propulsion system compared to commercial missions. To demonstrate the ability of XIPS© to meet the requirements of NASA science missions, L-3 Communications, Electron Technologies, Inc. (ETI) and the Jet Propulsion Laboratory (JPL) successfully performed throttling tests of the 25-cm thruster from 250 W to over 4.5 kW. The thruster performance in these tests met or exceeded that of the NSTAR 30-cm thruster over the NSTAR throttling range.[4]

The standard approach followed by NASA to qualify electric propulsion for the required throughput has been based largely on (long-duration) life tests, which can be costly and time consuming. For many

science missions, cost caps and launch timelines would simply prohibit such an approach to qualification. Presently, revised electric propulsion life-qualification approaches are being formulated that combine analytical and/or computational methods with (shorter-duration) wear tests. As a model case, a test is being performed at JPL to assess the wear mechanisms of the XIPS© discharge hollow cathode (DHC), and several diagnostic measurements of the plasma properties in these devices have already been obtained as part of the model-validation program. The wear and plasma data are being used to confirm the fidelity of existing cathode life models, which would in turn allow for the application of these models to, first, better understand the failure physics, and second, to determine the life expectancy of these devices for missions of interest to NASA without performing full life tests.[**]

The XIPS© DHC wear test has accumulated over 10,000 hrs,[5,6] and was scheduled to conclude at 15,000 hrs; the test may be continued however beyond the 15,000-hr mark depending on availability of resources. This paper reports on the analyses performed for this cathode and compares model results with plasma and wear data. We find that the 2-D computational model of the partially-ionized gas in these cathodes - dubbed OrCa2D[7,8] - predicts very well the plasma measurements, keeper voltage, and molybdenum (Mo)-keeper erosion profile observed in the XIPS© DHC after 5500 hrs of operation in HP mode. When the model is then applied to predict the erosion of a tantalum (Ta) keeper we show that erosion would be at least two orders of magnitude less compared to the Mo-keeper due the significantly lower sputtering yield of Ta. A Ta-keeper would therefore allow keeper lifetimes that greatly exceed the present requirements for NASA deep-space robotic missions. Ta-keepers are currently employed onboard the Dawn ion engine DHCs.

Table 1. Basic operational characteristics[††] of the DHC in the 25-cm XIPS©.

Operational Characteristics	*LP*	*HP*	*JPL wear test (after 5500 hrs)*
Discharge current, A	8.3	18.0	18-20
Discharge voltage, V	26.0	25.0	24-25
Mass flow rate, sccm	1.3	2.61	2.8

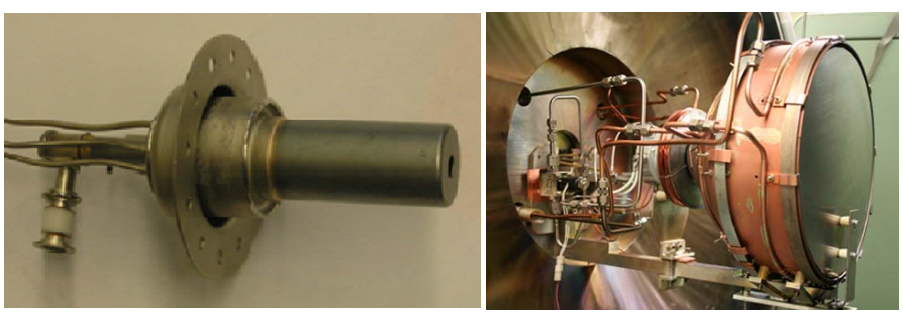

Fig. 2. Discharge hollow cathode (left)[5] and wear test setup (right) at JPL.

III. XIPS© Discharge Hollow Cathode Plasma and Wear Assessments

A. Basic Description of the Device and Related Data

The DHC investigated in this paper is the same cathode that is currently being wear-tested at JPL, and is part of a cathode assembly that has been provided by L-3 ETI (Fig. 2, left).[9] The assembly consists mainly of an impregnated tungsten emitter, a cathode tube and orifice plate, keeper electrode, heater and cathode-to-keeper insulator. Table 1 provides basic operational characteristics of the DHC in the 25-cm XIPS©. The cathode wear test is being conducted in a vacuum facility that is 1 m in diameter and 2 m in length, and is pumped by two 25-cm diameter cryogenic pumps. The base pressure is typically 1.3×10^{-4}

[**] By "full life test" we imply here a test that runs until cathode failure. In contrast, a "wear test" is in general of shorter duration and does not necessarily lead to full wear of a component or components and/or until cathode failure.

[††] Dimensions and other critical information are not shown hereinafter due to propriety restrictions.

Pa (1×10^{-6} Torr) and the range of xenon pressure during cathode operation is $2.7\text{-}4\times10^{-3}$ Pa ($2\text{-}3\times10^{-5}$ Torr). The DHC operates in a discharge chamber that has been designed to simulate the environment in a ring-cusp ion engine (Fig. 2, right). The DHC keeper plate is made of molybdenum-rhenium (Mo-Re). A more detailed description of the wear test facility and cathode performance over the first 4100 hrs is provided in Ref. 5. The recent status of the test is described in Ref. 6.

B. 2-D Computational Model of the Partially-Ionized Gas in the DHC

1. General description of the OrCa2D computational model

The two-dimensional computational model, Orificed Cathode (OrCa2D), used for DHC plasma simulations and wear predictions has been described in detail in previous articles[7,8] and will only be described briefly here. The model solves the conservation laws for three species present in the partially-ionized gas: electrons, xenon ions and xenon neutrals. In previous simulations of the NSTAR DHC plasma we computed a double-to-single ionization ratio of less than 3% along the keeper.[8] At such low ratios the exclusion of doubly-charged ions from the conservation laws will not affect a plasma solution that assumes singly-charged only, and this is shown to be the case for the XIPS DHC also in a later section. It is therefore assumed that only singly-charged ions are present and that the ionized species satisfy quasi-neutrality. Later, we also quantify the presence of Xe^{++} in the XIPS DHC and assess their effect on keeper erosion. The equations of continuity and momentum for ions, and the momentum equation for the electrons, are solved directly to yield the plasma particle density, ion and electron current densities. The combination of the electron and ion continuity equations yields the current conservation law, which is solved implicitly in OrCa2D to obtain the plasma potential. All relevant elastic and inelastic collision frequencies are included in the transport terms. Also, the models of the collision frequencies allow for the enhancement of the collision cross-sections from electrons with high drift energy.[10]

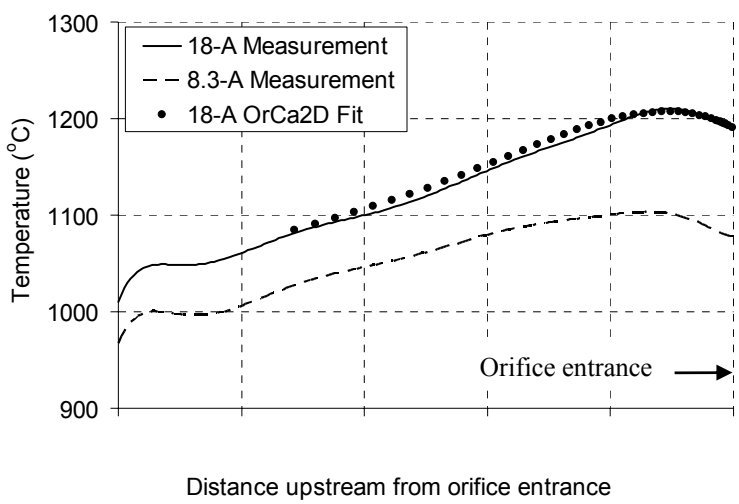

Fig. 3 Measured temperature along the XIPS© DHC emitter and fitted profile at the HP mode as used in the OrCa2D model.

The electron temperature is obtained from the electron energy transport equation, which includes thermal diffusion, energy losses due to ionization and the work done on the electrons by the electric field. The ions and neutrals are assumed to be in thermal equilibrium at temperature T_h inside the cathode and a single equation is employed for the conservation of energy of the heavy species. The orifice plate temperature is set equal to the peak emitter temperature. The keeper plate temperature is set to 400 °C based on previous test observations.[11] Sheath boundary conditions are applied at the cathode wall boundaries that include thermionic emission from the emitter based on a fit to the measured temperature profile,[5] as shown in Fig. 3.

The neutral gas density is determined by the neutral gas continuity equation that includes the zation source term for Xe^{+}. Inside the cathode the neutral gas viscous momentum equations are solved by a fluid approach, while downstream of the cathode orifice entrance a collisionless method is employed to obtain the neutral gas density.[10] The "fluid" and "collisionless" regions are coupled at the transition line, which in the XIPS© DHC simulations is located at the entrance to the cathode orifice. The numerical approach

for the neutral gas fluid momentum equation uses an upwind finite volume scheme by applying first-order upwind fluxes across each edge with no flux-limiting.

The computational region employed for the DHC simulations is illustrated in Fig. 4. It spans the cathode interior, cathode and keeper orifices, and the cathode's near-plume and far-plume/anode regions. The computational mesh consists mostly of rectangular cells inside the cathode but transitions to a generalized grid arrangement in the plume region. During the XIPS© DHC wear test the thruster magnetic field was emulated using current-carrying coils. This same magnetic field distribution has been implemented in the DHC numerical simulations also, and is shown in Fig. 4.

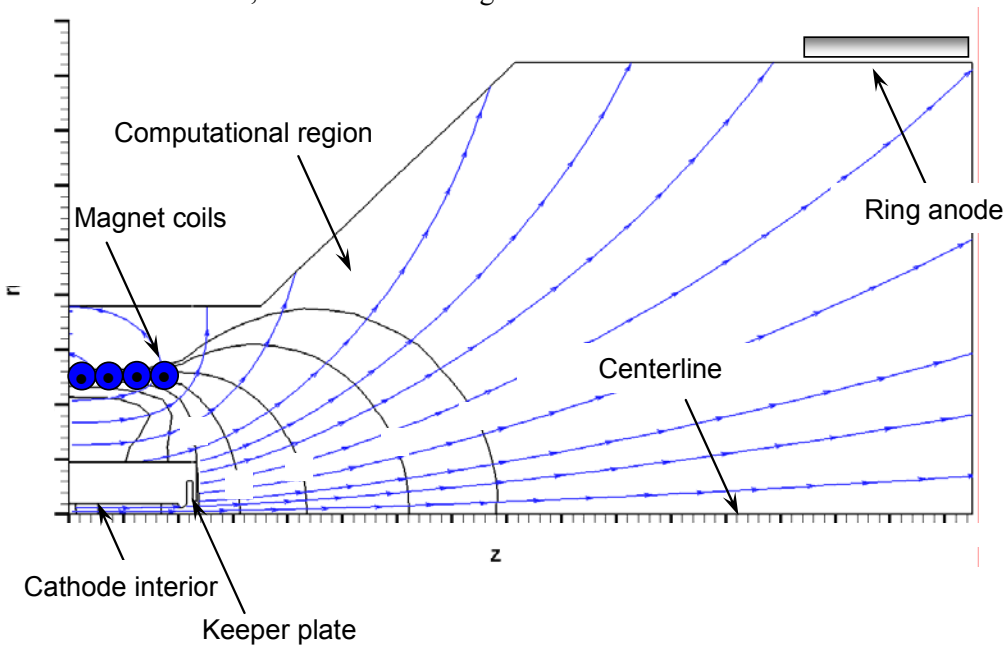

Fig. 4. Computational region for the XIPS© DHC numerical simulations showing (among others) location of the current-current coils and representative magnetic induction field (B) streamlines. Also shown are contours of constant B_z.

2. OrCa2D model enhancements

Two new advances have been made to the OrCa2D physics models. First, a new algorithm has been developed that allows for keeper current collection with self-consistent determination of the keeper voltage characteristics. The keeper current and sheath boundary conditions for the electron and ion current densities are specified as follows:

$$I_K = \oiint_{S_K} (\mathbf{j}_e + \mathbf{j}_i) \cdot d\mathbf{S}_K$$

$$\mathbf{j}_e \cdot \hat{\mathbf{n}} = \begin{cases} -j_{e,th}\, \mathrm{e}^{-q_e(\phi_p - V_K)/k_B T_e}, & \phi_p > V_K \\ -j_{e,th}, & \phi_p \le V_K \end{cases} \qquad \mathbf{j}_i \cdot \hat{\mathbf{n}} = \begin{cases} 0.607 q_e n_e \sqrt{k_B T_e / m_i}, & \phi_p > V_K \\ 0, & \phi_p \le V_K \end{cases} \tag{1}$$

where ϕ_p-V_K is the voltage drop across the sheath. The plasma potential at the grid cell center located adjacent to the wall boundary is denoted by ϕ_p. In the new OrCa2D algorithm an iterative procedure has been added that allows for the determination of V_K based on a prescribed value of the keeper current. When $\phi_p \le V_K$ it is assumed that the sheath is (fully) ion-repelling and no ion flux to the wall is allowed, and electron collection is not allowed to exceed the electron thermal flux, $j_{e,th}=n_e(8k_BT_e/\pi m_e)^{1/2}/4$.

Second, a revised anomalous resistivity model has been employed that determines (rather than assumes) the coefficient and ratio of electron-to-ion temperature ratio (T_e/T_i) based on a sonic condition for the electrons. Specifically, the anomalous resistivity η_α is given by,

$$\eta_a = \frac{m_e \nu_a}{q_e n_e}, \qquad \nu_a = a' \frac{u_e}{u_{T,e}} \omega_{pe} \tag{2}$$

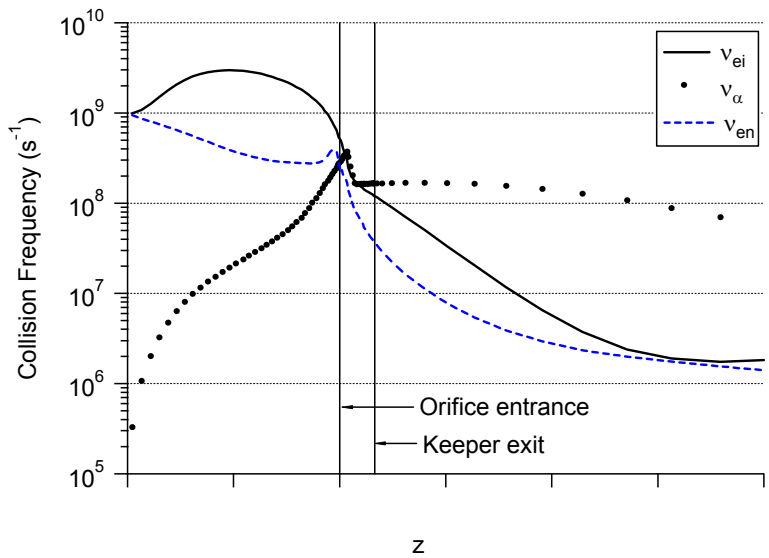

Fig. 5. Comparison of the electron collision frequencies in the XIPS© DHC along the axis of symmetry.

where $\alpha' \equiv \alpha T_e/T_i$, and α' is now determined by iteration such that the maximum Mach number of the electron flow, $M_e = u_e/u_{T,e}$, does not exceed unity. The computed M_e-contours for the XIPS© DHC in HP mode are shown in Fig. 6; for the case shown it is determined that $\alpha' = 1.879\times10^{-3}$. The expression in Eq. (2), with coefficient α being a proportionality constant, has been based on the well-known Sagdeev formula for ion-acoustic turbulence[12] and in previous DHC simulations it was implemented with an *ad hoc* cap because the ratio T_e/T_i in the plasma-fluid simulation becomes exceedingly high. This is because the transformation of wave energy into heat of the ion population is not yet self-consistently taken into account since the energy transfer mechanism is not yet known. As an alternative to a cap on the resistivity we propose here that if electrons are extracted from the cathode at a Mach number that exceeds unity wave motion that gets excited in the plasma saturates in short time scales compared to ion motion, into (low-frequency) ion-acoustic turbulence to retain the electron Mach number to values below unity. The saturation occurs by the pumping of wave energy into electron and ion heating. The approach is phenomenological and requires further experimental validation (extended to measurements beyond those presented herein) and rigorous mathematical confirmation. Specifically, the simplifying assumptions associated with Eq. (2) in the presence of an applied magnetic field, the manner with which T_e/T_i is accounted for in the conservation laws, and possible deviations from the Maxwellian velocity distribution function must be investigated further. Nevertheless, based on comparisons with the existing plasma data, the computed steady-state solution captures well the overall trends associated with the time-averaged plasma measurements both axially and radially (near the keeper), as it will be shown in the next section. Later, it will also be shown that the erosion of the keeper can be reduced by more than two orders of magnitude with a change in material, so that the impact of the aforementioned uncertainties in the steady-state solution is negligible.

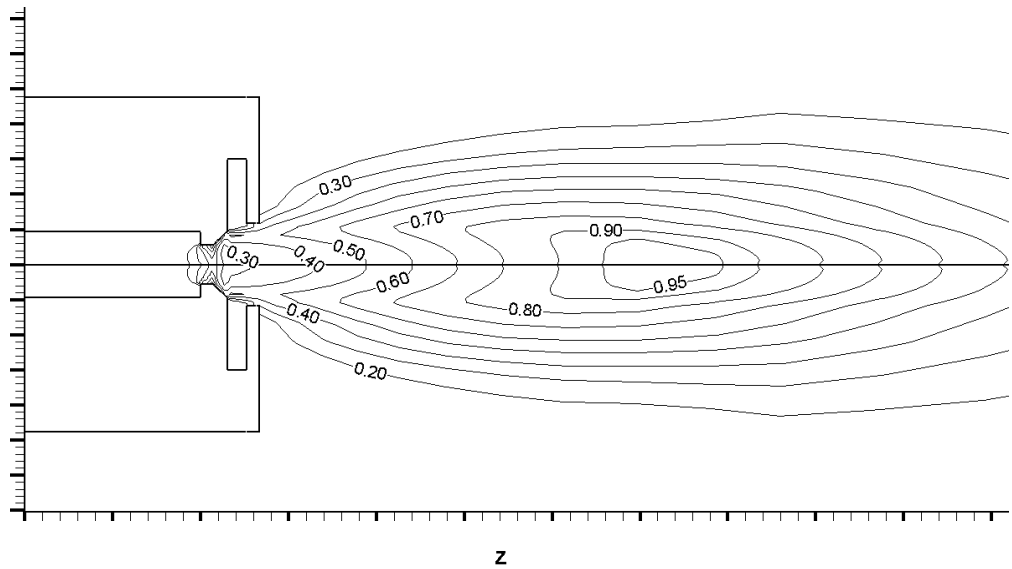

Fig. 6. Contours of electron Mach number $u_e/u_{T,e}$ in the DHC near-plume.

C. Model Results and Validation with the Test Data

1. Comparisons between OrCa2D results, plasma measurements and circuit characteristics

In this section we present both axial and radial comparisons between the OrC2D results and plasma measurements taken at JPL facilities. Both single Langmuir and emissive probes have been used to obtain the data. A description of the diagnostics and experiment setup has been reported in previous articles.[13,14] The axial profiles of the plasma density and potential in the cathode plume are compared in Fig. 7. Discrepancies in the axial gradients are noticeable and are largely a consequence of the fixed ratio of T_e/T_i assumed in the anomalous resistivity model throughout the plume plasma. Moreover, the precise evolution of the plasma beyond a few keeper diameters from the keeper exit, beyond the electron sonic point, is not yet thoroughly understood. Nevertheless, based on the direct comparisons with plasma measurements below, the time-averaged conditions in the vicinity of the keeper are determined by OrCa2D to be within the experimental uncertainty: at the keeper exit, on-axis, the measured plasma density and the computed value are within a factor of two (Fig. 7, left), the on-axis plasma potential is within 4.4% of the measured value nearest to the keeper exit (Fig. 7, right), and radially, a few mm downstream of the keeper surface the computed value is within 7.5% of the time-averaged measurement (Fig. 8).

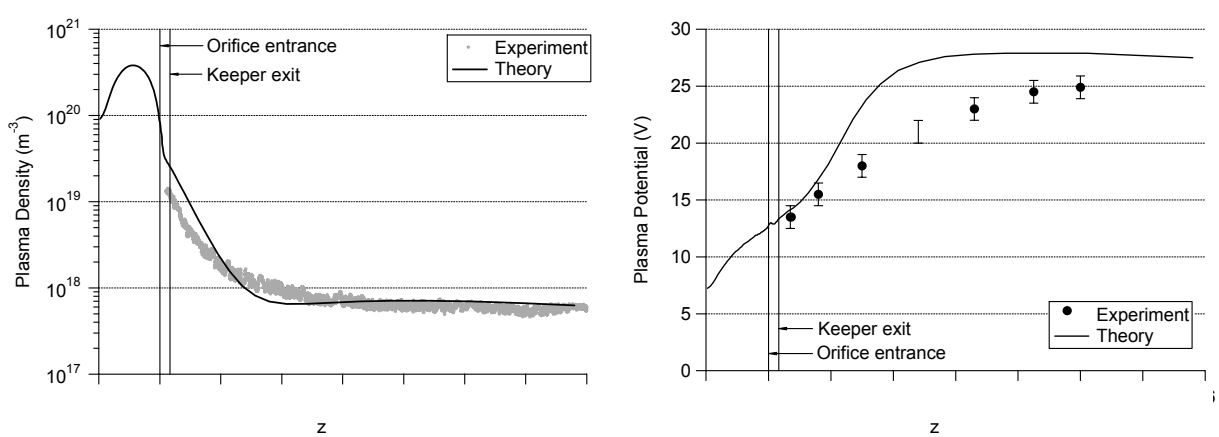

Fig. 7. Comparison of measured and computed plasma properties along the axis of symmetry. Left: Plasma number density. Right: Plasma potential.

In the radial direction, the computed plasma potential and electron temperature are plotted in Fig. 8 at the axial location of the keeper exit. Also plotted are plasma potential measurements taken with a radially-scanning emissive probe that allowed for the detection of plasma oscillations. As with the axial Langmuir probe, the emissive probe was driven pneumatically into the plasma. The probe signal was fed to a high-impedance, high-frequency circuit and to a buffer amplifier to detect oscillations in the signal. The system was capable of detecting frequencies up to 1 MHz. Two sample rates are plotted in Fig. 8, 500 kHz and 20 kHz, to distinguish between regions dominated by high oscillation frequencies and those with low frequencies. The oscillation amplitude appears to peak at a radial location that is about ¼ of the keeper face above the inner radius, which is where the model also predicts the highest electron temperature. As it will be shown in the next section, capturing the radial dependence of the oscillation amplitude through the electron temperature is critical since the erosion of the keeper is driven largely by the enhancement of the energy of ions bombarding the wall as a result of the oscillations. That is, for a fixed time-averaged plasma potential the erosion rate is highest when the oscillations are of the highest amplitude. In the erosion model the amplitude is accounted for through "A": the peak value (measured in multiples of $k_B T_e$) that the plasma potential reaches above its time-averaged value.

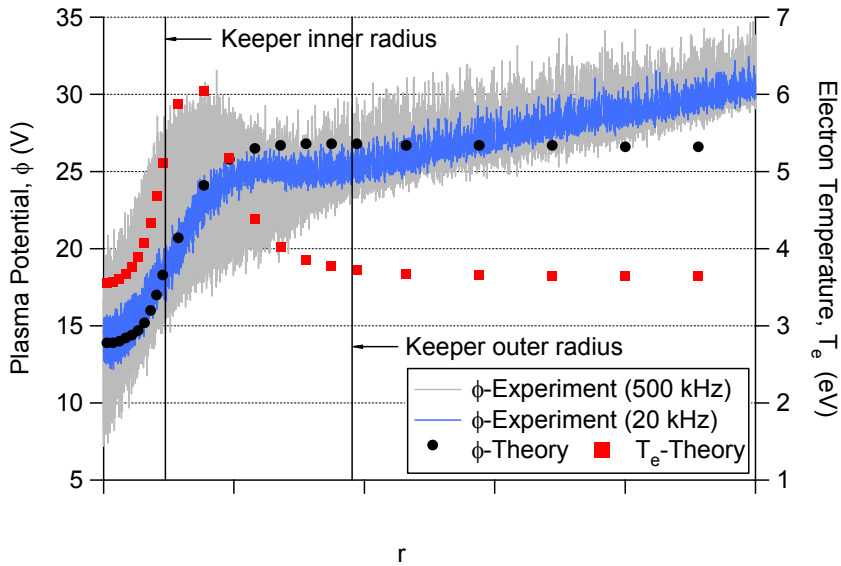

Fig. 8. Measured and computed plasma properties as a function radius near the keeper plume-facing surface.

Finally, Fig. 9 shows the computed keeper circuit characteristics and Fig. 10 depicts the observed trends of the wear test during which the cathode was operated at a discharge current that ranged 18-21 A. The various segments shown in Fig. 10 are described in detail in Refs 5 and 6. For the nominal keeper current of 1 A in HP-mode OrCa2D predicts V_K=7.1 V, which is within ~5% of the latest (5500-hr) value of the keeper voltage observed in the wear test, 7.5 V.

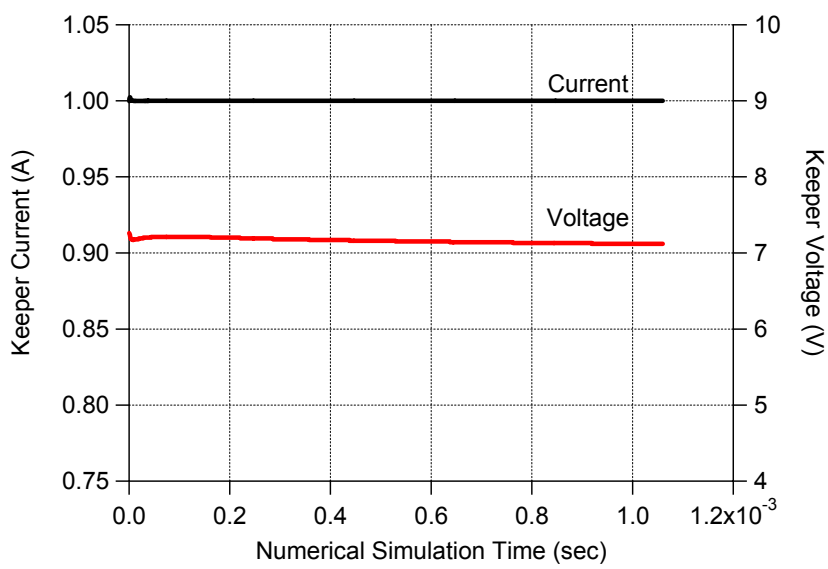

Fig. 9. Keeper current and voltage characteristics as computed by OrCa2D. An iteration algorithm determines the voltage V_K given the current I_K.

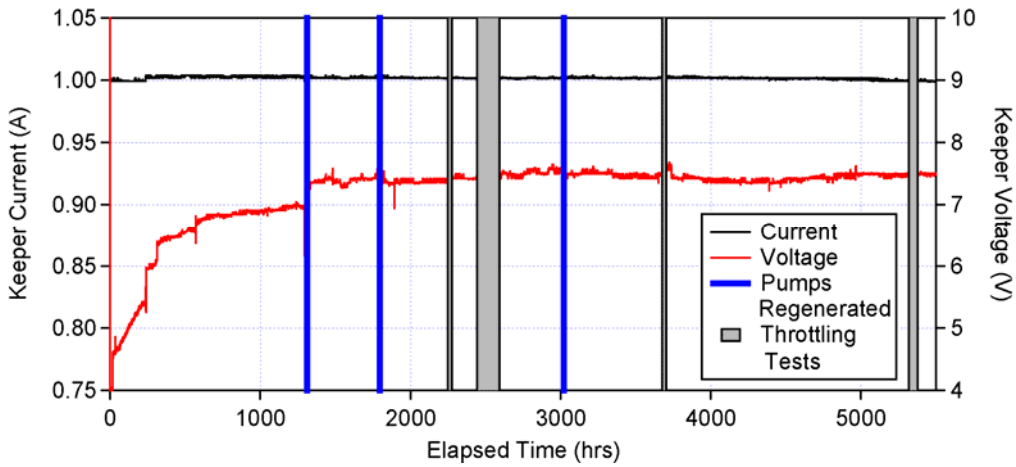

Fig. 10. Keeper current and voltage characteristics in HP cathode operation observed during the cathode wear test at JPL. The steady-state computed value of the keeper voltage is 7.1 V and the observed value after 5500 hrs of operation is 7.5 V.

2. Predictions of keeper erosion and comparisons with wear-test observations

In this section we apply to the XIPS© DHC the same physics-based algorithm[8] used to predict the erosion of the DHC in the NSTAR 30-cm ion thruster and the same sputtering yield data (Fig. 11).[15,16] The model asserts that the sputtering yield associated with the keeper material is effectively enhanced by the ion-acoustic turbulence that takes place in the plasma adjacent to the keeper face, because the ions that bombard the surface acquire additional energy from such wave motion. The effective ion energy at any given radial location adjacent to the keeper is assumed to consist of a time-averaged value ε_i' and a sinusoidal term with amplitude Ak_BT_e representing the enhancement by the plasma waves:

$$\varepsilon_i = \varepsilon_i' + Ak_BT_e \cos\theta \,. \tag{3}$$

Noting that in such case the instantaneous sputtering yield based on the time-averaged ion energy does not equal the time-averaged yield based on the instantaneous ion energy, we estimate the latter by averaging over all angles in the range 0-2π (with 1-degree increments) as given by Eq. (4). The consequence of Eqs. (3) and (4) is to increase significantly the sputtering yield (by a few orders of magnitude in some cases depending on the wave amplitude), and to reduce the sensitivity of the yield on the ion energy (Fig. 11).[8]

$$\overline{Y} = \frac{\int_0^{2\pi} Y(\varepsilon_i)\, d\theta}{\int_0^{2\pi} d\theta} \tag{4}$$

The left plot in Fig. 12 depicts the erosion profile of the XIPS© DHC Mo-keeper as observed after ~5500 hrs of wear testing at JPL. The top photograph in Fig. 12-right is a front view of the cathode at beginning of life (BOL) and the bottom is an angled-view picture taken after ~1300 hrs of operation showing a noticeably textured keeper-plate front surface. The computed plasma potential and ion flux to the keeper are used to predict the erosion of the Mo-keeper, compare with the observed profile, and then predict the erosion of a keeper made of tantalum (Ta), which has a considerably lower sputtering yield compared to molybdenum. The fits shown in Fig. 11 (extended to low-energy values where no data exist) have been used in the erosion calculations. The normalized spectroscopic data for the Ta yield have been used in these calculations.

The results of the erosion calculations are shown in Fig. 13. The Mo-keeper results used the same wave amplitude, A=4.5, that was used in the NSTAR DHC erosion predictions and are shown in the left. The choice of A here requires further explanation. A detailed empirical study[17] of the plasma dynamics in the near-plume of the NSTAR DHC showed that the presence of turbulent oscillations in this region persisted for all operating conditions. The NSTAR DHC has the same cathode tube diameter, keeper orifice and keeper outer diameter as the XIPS DHC, but the cathode orifice diameter is 2¼ smaller in the NSTAR DHC. The range of frequencies observed was relatively large, 0.1-2 MHz, and the observed fluctuation level varied; the maximum amplitude that was measured exceeded 5 times the local electron temperature. These fluctuations were found to be incoherent, that is, their frequency (among others) changed randomly. Although some general trends regarding frequency, amplitude, operating condition and cathode geometry have been reported[17] the random nature of these oscillations challenges theoretical as well as empirical means by which unambiguous correlations between oscillation amplitudes and geometrical or operational variables may be established. Moreover, in light of the strong dependence of the sputtering yield on the ion energy, which is largely enhanced by the wave motion, the accuracy with which any such correlations can be established is unlikely to yield erosion predictions that are better than a factor of two. So, here we choose the value A=4.5 because it is close to the highest amplitude factor that has been measured in these DHCs, thereby yielding the worst-case scenario for erosion of the XIPS DHC, and because this value closely re-produced the erosion profile that was observed in the NSTAR DHC. To assess the sensitivity of the erosion prediction on our choice of A, an erosion profile for a value that exceeds the maximum observed is also presented. It will be shown later that the uncertainty in the prediction of A has negligible impact on our ability to demonstrate that the expected life of the keeper is more than adequate for NASA science missions because a change in the keeper material from Mo to Ta, for the same operating conditions, yields an erosion rate that is at least two orders of magnitude less than Mo.

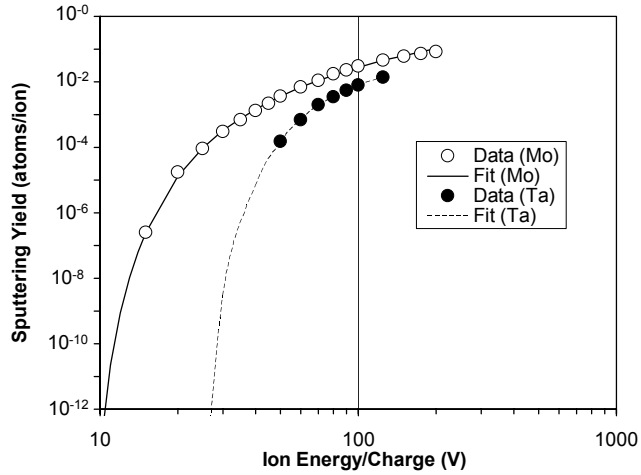

Fig. 11. Sputtering yield $Y(\varepsilon_i)$ for Mo and Ta. The experimental uncertainty for ion energy ε_i<60V is ~20-30% for Mo and approximately ~40% for Ta.

For A=4.5, the largest discrepancy between prediction and observation is ~50% and occurs near the inner radius of the keeper orifice, at the front face, where the highest-amplitude oscillations are observed (see Fig. 8). As alluded to above, due to the inherent randomness associated with the incoherent fluctuations, the precise amplitude of the oscillations in this region is uncertain and may in fact vary throughout the operation of the cathode. To quantify the sensitivity of the result on A, the predicted profile for amplitude that is one k_BT_e higher than the original value is plotted in Fig. 13. It should also be noted that the enlargement of the keeper orifice by the erosion usually leads to accelerated erosion rates because the plasma potential increases in this region. This effect was shown in previous work with the NSTAR DHC.[8] Loss of electron collisionality as a result of the enlargement would also lead to enhanced plasma oscillations in this region that would further increase the erosion rate. Using the same wave amplitude, A=4.5, the predicted erosion profiles for the Mo-keeper and a Ta-keeper are compared in Fig. 13 after 85 khrs. The comparison shows that the erosion of a Ta-keeper is more than two orders of magnitude less than that of a Mo-keeper at the plate outer face, and more than three orders of magnitude less at the keeper orifice. To cause the same erosion in the Ta-keeper after 85 khrs, the amplitude factor A would have to be 10-12 k_BT_e, implying peak plasma potentials of almost 100 V; such values have never been empirically observed in the NSTAR or XIPS DHCs.

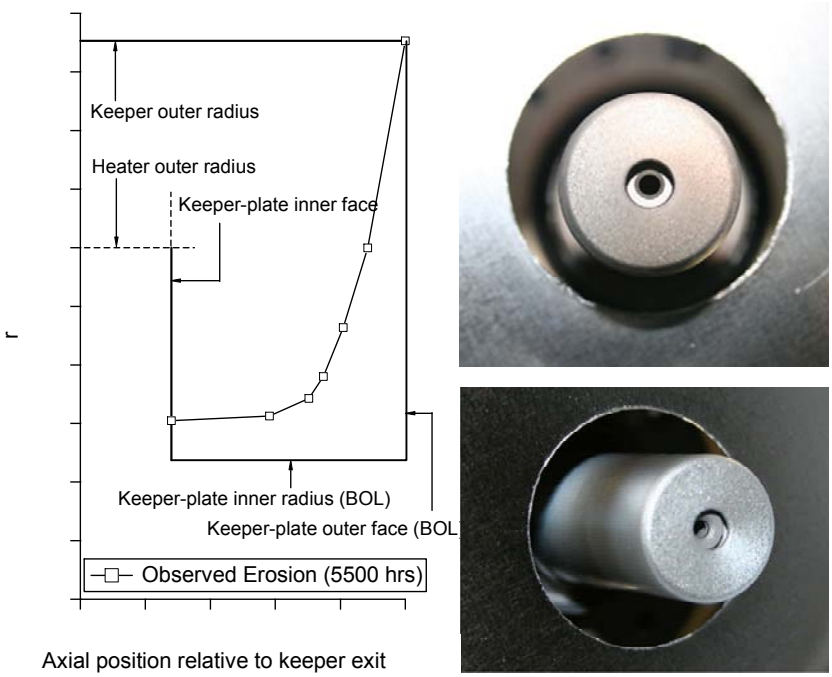

Fig. 12. Left: Keeper geometry and observed erosion after 5.5 khrs (Note: Increments on the abscissa do not equal those on the ordinate). Top right: DHC and keeper assembly at BOL. Bottom right: DHC and keeper assembly after 1320 hrs of operation.

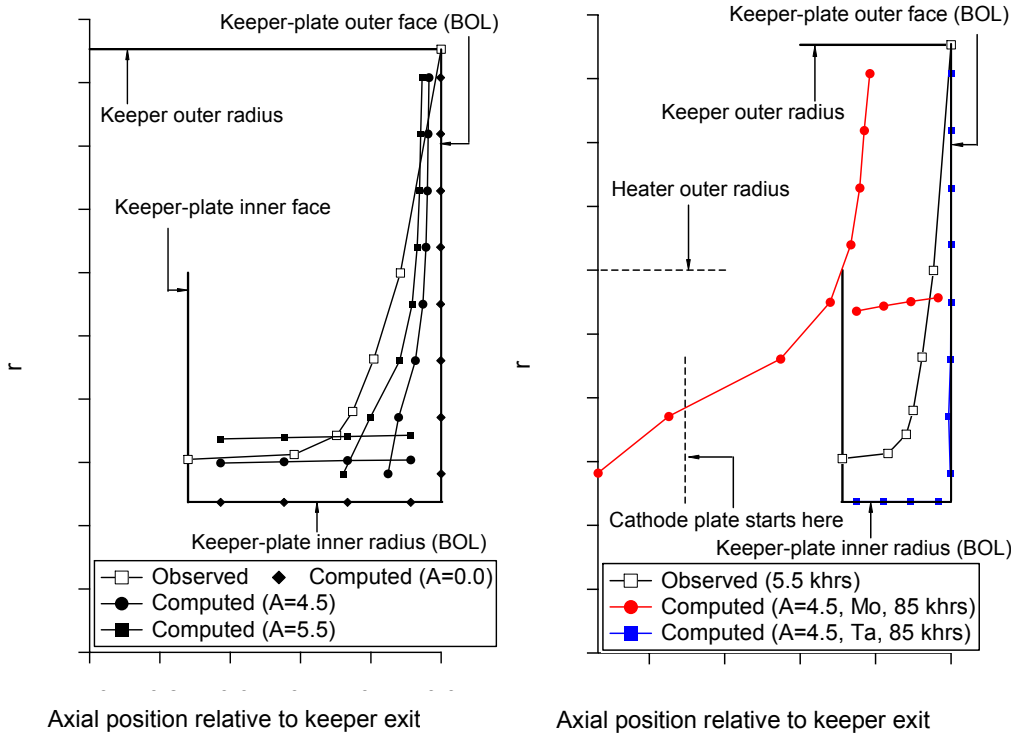

Fig. 13. Left: Observed and predicted erosion profiles for the Mo-keeper after 5.5 khrs. Right: Predicted erosion profiles for Mo-keeper and Ta-keeper after 85 khrs. (Notes: [1] The predicted profiles do not take into account the accelerated erosion that occurs as the keeper orifice is enlarged.[8] Thus, complete erosion of the Mo-keeper is likely to occur much sooner than 85 khrs of operation in HP mode. [2] Increments on the abscissa do not equal those on the ordinate).

3. Effect of doubly-charged ions (Xe^{++})

The double-to-single ion current ratios in the ELT ion engine have been reported to be in the range of 0.02-0.2[18] (but the values near the keeper are unknown), and typical values of the electron temperature near the keeper may be as high as ~6eV. Since the model computes self-consistently all the variables associated with ionization it is possible to determine the ratio of double and single ionization rates, $\ddot{n}/\dot{n}$ near the keeper surface for the XIPS DHC, and to assess the impact of Xe^{++} on the keeper erosion.

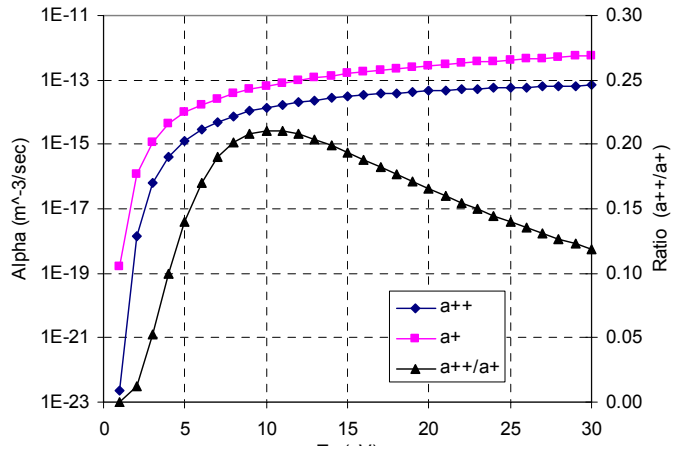

Fig. 14. Ionization α's for Xe+ and Xe++.

Based on measured Xe^{++} ionization collision cross-sections[19] for the $e+Xe^{+} \rightarrow Xe^{++}$ reaction that have been averaged over a Maxwellian distribution function, we determine the ratio of the ionization rates given in Eq (1) below. A comparison between α^{+} and α^{++} is given in Fig. 14. The ionization ratio in the keeper region is shown in Fig. 15 (left). The plot shows that $\ddot{n}/\dot{n}$ does not exceed 1.53% near the keeper surface but can be higher (~4%) downstream. To quantify the flux of Xe++ striking the keeper the solution of the 2-D flow of these ions must obtained.

$$\begin{aligned} \dot{n} &= n_e n_0 \alpha^{+}, \quad \alpha^{+} \equiv \left\langle \sigma^{+} u_e \right\rangle \\ \ddot{n} &= n_e n_i^{++} \alpha^{++}, \quad \alpha^{++} \equiv \left\langle \sigma^{++} u_e \right\rangle \end{aligned} \tag{1}$$

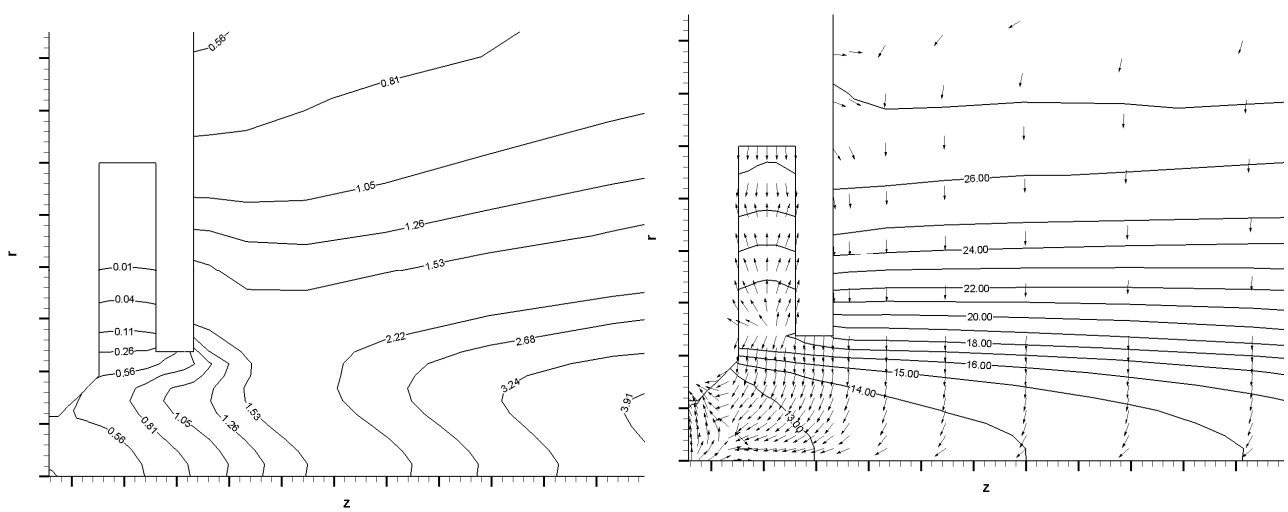

Fig. 15. Left: %Double-to-single ionization rate ratio, $\ddot{n}/\dot{n}$. Right: Contours of plasma potential overlaid by electric field unit vectors. (Note: electric field solution determined based on assumption of singly-charged ionized plasma).

We begin with the general momentum equations for the three charged species. For slow-moving particles the inertia terms may be neglected to obtain for electrons, Xe^{+} and Xe^{++} respectively:

$$0 = -n_e e\mathbf{E} - \nabla p_e - n_e m_e \nu_{ei}^{+}\left(\mathbf{u}_e - \mathbf{u}_i^{+}\right) - n_e m_e \nu_{ei}^{++}\left(\mathbf{u}_e - \mathbf{u}_i^{++}\right) - n_e m_e \nu_{en} \mathbf{u}_e \tag{2}$$

$$0 = n_i^+ e\mathbf{E} - \nabla p_i^+ - n_i^+ m_i \nu_{ie}^+ \left(\mathbf{u}_i^+ - \mathbf{u}_e\right) - n_i^+ m_i \nu_{ii}^+ \left(\mathbf{u}_i^+ - \mathbf{u}_i^{++}\right) - n_i^+ m_i \nu_{in}^+ \left(\mathbf{u}_i^+ - \mathbf{u}_n\right) \tag{3}$$

$$0 = 2n_i^{++} e\mathbf{E} - \nabla p_i^{++} - n_i^{++} m_i \nu_{ie}^{++} \left(\mathbf{u}_i^{++} - \mathbf{u}_e\right) - n_i^{++} m_i \nu_{ii}^{++} \left(\mathbf{u}_i^{++} - \mathbf{u}_i^+\right) - n_i^{++} m_i \nu_{in}^{++} \left(\mathbf{u}_i^{++} - \mathbf{u}_n\right). \tag{4}$$

We may re-arrange by adding Eqs. (2)+(3) and by applying the condition for charge neutrality in the plasma,

$$n_e = \sum_s Z_s n_s^{Z_s+} = n_i^+ + 2n_i^{++} \tag{5}$$

to obtain an expression for the singly-charge ion flux as follows:

$$\mathbf{\Gamma}_i^+ = \frac{-2en_i^{++}\mathbf{E}}{m_i\left(\nu_{ii}^+ + \nu_{in}^+\right)} - \frac{\nabla\left(p_e + p_i^+\right)}{m_i\left(\nu_{ii}^+ + \nu_{in}^+\right)} + \frac{m_e}{m_i}\frac{\nu_{en} + \nu_{ei}^{++}}{\nu_{ii}^+ + \nu_{in}^+}\frac{\mathbf{j}_e}{e} + \frac{\nu_{in}^+ n_i^+ \mathbf{u}_n}{\nu_{ii}^+ + \nu_{in}^+} + \left(\frac{n_i^+}{n_i^{++}}\frac{\nu_{ii}^+}{\nu_{ii}^+ + \nu_{in}^+} + \frac{n_e}{n_i^{++}}\frac{m_e}{m_i}\frac{\nu_{ei}^{++}}{\nu_{ii}^+ + \nu_{in}^+}\right)\mathbf{\Gamma}_i^{++} \tag{6}$$

where the ion-ion collision frequency for Xe^+ striking a Xe^{Z+} is

$$\nu_{ii}^+ = \frac{n_i^{Z+} Z^4 e^4 \ln\Lambda}{3\sqrt{2}\varepsilon_0^{\,2} m_i^{\,2}}\left(\frac{m_i}{2\pi e T_i}\right)^{3/2} \approx 4.8\times 10^{-14} n_i^{Z+} Z^4 \sqrt{\frac{m_p}{m_i}}\frac{\ln\Lambda}{T_i^{3/2}} s^{-1} \tag{7}$$

with the ion temperature expressed in eV. We recall the equation for the ion current density assuming singly-charged ions only (n_e=n_i^+)

$$\mathbf{\Gamma}_i^+ = -\frac{\nabla\left(p_e + p_i^+\right)}{m_i \nu_{in}^+} + \frac{m_e}{m_i}\frac{\nu_{en}}{\nu_{in}^+} e^{-1}\mathbf{j}_e + n_i^+ \mathbf{u}_n \tag{8}$$

and note the appearance of the first and last terms in the right-hand-side of Eq. (6) as well as the two new collision frequencies for e→Xe^{++} and Xe^+→Xe^{++}. We note that the Xe^+→Xe^{++} collision frequency is proportional to n_i^{++} and is therefore much smaller than the Xe^+→Xe (charge-exchange) frequency. It can easily be shown then that for the singly-charged ion flow as well as for all other relevant plasma properties the presence of Xe++ of a few percent relative to Xe+ will not alter the existing solution that is based on the assumption of a singly-ionized plasma. We therefore compute the Xe++ ion flow based on the existing solution for the plasma by solving two additional conservation equations: Xe++ continuity,

$$\frac{\partial n_i^{++}}{\partial t} + \nabla\cdot\mathbf{\Gamma}_i^{++} = \ddot{n} \tag{9}$$

and Xe++ momentum. We use Eq. (4) to obtain an expression for the flux of doubly-charged ions as follows:

$$\begin{aligned}
&0 = 2n_i^{++} e\mathbf{E} - \nabla p_i^{++} - n_i^{++} m_i \nu_{ie}^{++} \left(\mathbf{u}_i^{++} - \mathbf{u}_e\right) - n_i^{++} m_i \nu_{ii}^{++} \left(\mathbf{u}_i^{++} - \mathbf{u}_i^+\right) - n_i^{++} m_i \nu_{in}^{++} \left(\mathbf{u}_i^{++} - \mathbf{u}_n\right) \\
&m_i \nu_{ie}^{++} n_i^{++} \mathbf{u}_i^{++} + n_i^{++} m_i \mathbf{u}_i^{++} \left(\nu_{ii}^{++} + \nu_{in}^{++}\right) = 2n_i^{++} e\mathbf{E} - \nabla p_i^{++} + n_i^{++} m_i \nu_{ie}^{++} \mathbf{u}_e + n_i^{++} m_i \nu_{ii}^{++} \mathbf{u}_i^+ + n_i^{++} m_i \nu_{in}^{++} \mathbf{u}_n \\
&n_e m_e \nu_{ei}^{++} = n_i^{++} m_i \nu_{ie}^{++} \rightarrow \mathbf{\Gamma}_i^{++} = \frac{2n_i^{++} e\mathbf{E}}{\nu_i^{++} m_i} - \frac{\nabla p_i^{++}}{\nu_i^{++} m_i} - \frac{m_e}{m_i}\frac{\nu_{ei}^{++}}{\nu_i^{++}}\frac{\mathbf{j}_e}{e} + n_i^{++}\left(\frac{\nu_{ii}^{++}}{\nu_i^{++}}\mathbf{u}_i^+ + \frac{\nu_{in}^{++}}{\nu_i^{++}}\mathbf{u}_n\right)
\end{aligned} \tag{10}$$

where we have defined the total collision frequency for the Xe++ flow as,

$$\nu_i^{++} \equiv \left(\nu_{ii}^{++} + \nu_{in}^{++} + \frac{n_e}{n_i^{++}} \frac{m_e}{m_i} \nu_{ei}^{++} \right) \tag{11}$$

In contrast to the case of singly-charged ions we note that ν_{ii}^{++} is proportional to the singly-charged ion density n_i^+. We provide a quantitative comparison between ν_{ii}^{++} and ν_{in}^+ along the axis of symmetry in Fig. 16 (ν_{in}^{++} is estimated to be ~$0.7\nu_{in}^+$ based on collision cross-sections measurements of Miller and Pullins[20]). Two results are shown for ν_{ii}^{++} to provide a range that represents the possible ion temperatures that can exist in the cathode. The comparison in Fig. 16 is important for two reasons: first, the ion-ion collision frequency cannot be neglected in the Xe^{++} flow regardless of whether T_i=T_n or T_i=T_e, and second, if the ions are in thermal equilibrium with the neutrals then the doubly-charged ion flux is largely driven by the singly-charged ion flux, as shown by the comparison of the two flow fields in Fig. 17, since the importance of the remaining terms in Eq. (10) is greatly reduced. For the case of ions in thermal equilibrium with electrons, the ion-ion collision frequency may be comparable to the charge-exchange collision frequency and the remaining terms may be greater. The latter case is in consideration of previous hypotheses that the ion temperature may be greater than the neutral gas temperature as a result of the ion-acoustic wave motion. The contribution of the Xe++ to the erosion is shown in Fig. 18 and all relevant values at a representative location (Point 1 on Fig. 18) are tabulated in Table 3.

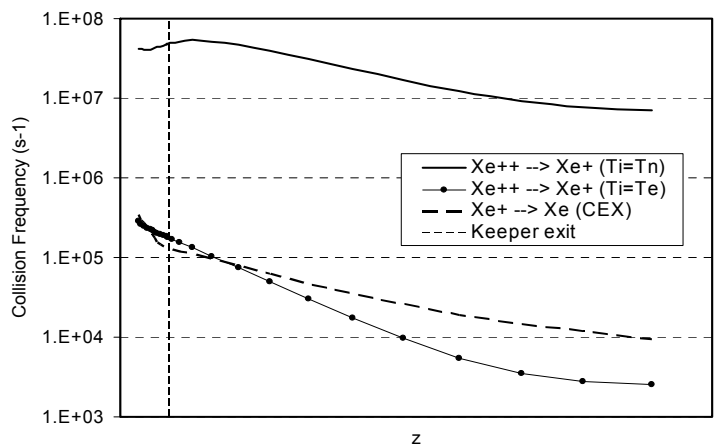

Fig. 16. Collision frequencies for the heavy species along the axis of symmetry

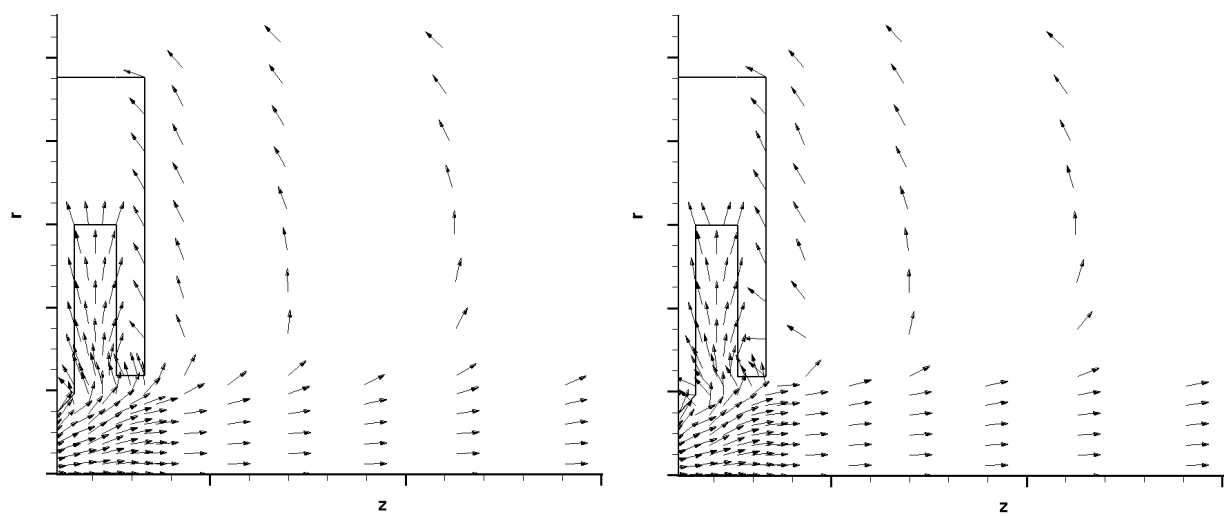

Fig. 17. Unit vectors of the ion flux in the vicinity of the keeper. Left: Singly-charge xenon (Xe^+). Right: Doubly-charged xenon (Xe^{++}).

Table 2. Quantities relevant to erosion at Point 1.

Property	*Value*
$\Gamma_{i,\perp}^{+}$ (m^{-2}s^{-1})	1.665×10^{21}
$\Gamma_{i,\perp}^{++}$ (m^{-2}s^{-1})	3.127×10^{19}
$\varepsilon_i'^{+} = \phi - V_K$ (V)	13.169
$\varepsilon_i'^{++} = 2\phi - V_K$ (V)	33.437
$\overline{Y}(\varepsilon_i^{+})$ (atoms/ion)	2.778×10^{-4}
$\overline{Y}(\varepsilon_i^{++})$ (atoms/ion)	2.045×10^{-3}
$\dfrac{\Gamma_{i,\perp}^{++}\overline{Y}(\varepsilon_i^{++})}{\Gamma_{i,\perp}^{++}\overline{Y}(\varepsilon_i^{++}) + \Gamma_{i,\perp}^{+}\overline{Y}(\varepsilon_i^{+})}\%$	12.143

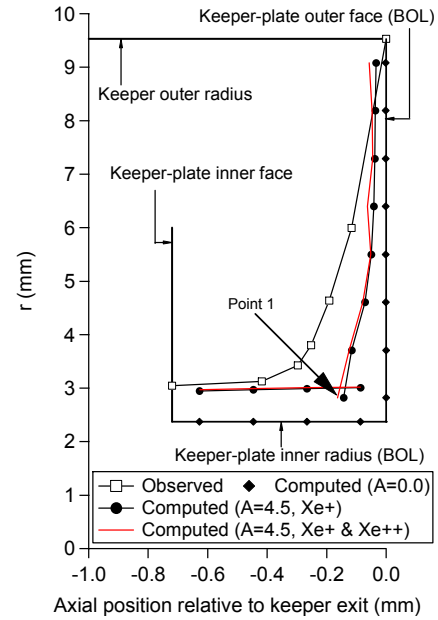

Fig. 18. Comparison of erosion profiles for Xe+ only and for Xe+ and Xe++ ion flow.

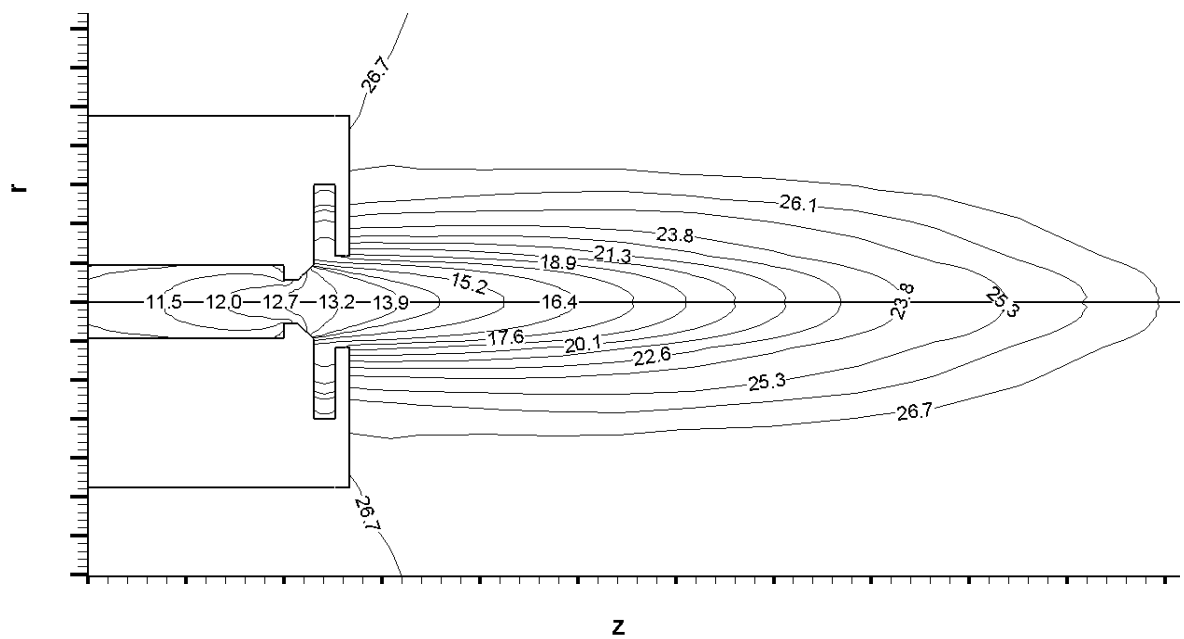

Fig. 19. Contours of the steady-state plasma potential in the XIPS© DHC at HP-mode operation.

4. Cathode orifice

Finally, when the same erosion model is applied to the cathode orifice, with A=4.5 and Xe+ only, we predict comparable erosion rates between the keeper orifice (~1×10^{-4} mm/hr) and the cathode orifice (~0.85×10^{-4} mm/hr), with the plasma potential ranging between 12 V and 13 V (Table 3) in the cathode orifice region (Fig. 19), and the cathode voltage V_C taken to zero. However, enhancement of the erosion by plasma oscillations is unlikely in this region since classical collisions begin to prevail over wave motion in determining electron transport as suggested by the comparison of "collision" frequencies along the axis of symmetry in Fig. 5; under this scenario plasma waves would be damped. For A=0 the predicted erosion rate in the cathode orifice is more than three orders of magnitude less than for A=4.5. It is however probable that enhanced erosion due to plasma oscillations will occur if significant erosion of the keeper is permitted. The latter can be avoided by using a Ta-keeper.

Table 3. Comparison of conditions and erosion rates at the cathode and keeper orifices.

Computed conditions	*Cathode orifice (V_C=0 V)*	*Keeper orifice (V_K=7.1 V)*
Ion number density, m^{-3}	$3.95\text{-}6.93\times10^{19}$	$0.49\text{-}0.5\times10^{19}$
Plasma potential, V	11.4-12.0	17.3-17.6
Electron temperature, eV	2.54-2.78	4.65-4.71
Erosion rate (A=0.0), mm/hr	$0.29\text{-}1.2\times10^{-8}$	$0.98\text{-}6.4\times10^{-12}$
Erosion rate (A=4.5), mm/hr	$8.2\text{-}8.7\times10^{-5}$	$1.1\text{-}1.2\times10^{-4}$

IV. Conclusions

The OrCa2D computational model of the partially-ionized produced by hollow cathodes has been applied to predict the plasma conditions and the erosion of the electrodes in the 25-cm XIPS DHC after 5500 hrs of wear testing. The OrCa2D predictions of the plasma conditions at various cathode locations have been compared with measurements during operation in HP mode. Considering the uncertainty associated with the electron transport in the cathode plume and the rudimentary resistivity model used to account for plasma oscillations, the comparison appears to be very good. This suggests that the proposed global picture regarding the saturation of wave motion into low-frequency turbulence to reduce the electron Mach number below the sonic conditions, while retaining a relatively uniform ratio of electron-to-ion temperature in the near plume, is not unfeasible in these devices. OrCa2D also predicts within 5% the keeper voltage for the nominal keeper current of 1 A.

In regards to wear, the life model based on the OrCa2D plasma results predicts closely the erosion profile that has been observed on the keeper in an ongoing wear test of the DHC, and is within ~50% of the maximum face erosion when the wave amplitude factor A is of the same value (4.5) as that used to predict the erosion of the keeper in the DHC of the NSTAR 30-cm ion engine. The value A=4.5 has been chosen in these calculations because it is close to the highest amplitude factor that has been measured in these DHCs, thereby yielding the worst-case scenario for erosion of the XIPS DHC, and because this value closely re-produced the erosion profile that was observed in the NSTAR DHC. Future work will focus on the determination of a theoretical limit for the maximum value of the wave amplitudes to reduce the uncertainty and improve our understanding, thereby further reducing the risk associated with keeper wear. From a more practical viewpoint, such work would be merely academic: this paper suggests that the uncertainty in the prediction of A has negligible impact on our ability to demonstrate that the expected life of the keeper is more than adequate for NASA science missions because a change in the keeper material from Mo to Ta, for the same operating conditions, yields an erosion rate that is at least two orders of magnitude less than Mo.

In summary, the analysis presented in this paper accomplishes two main goals. First, it raises our confidence in the 2-D model and on our understanding of the keeper wear mechanism by reproducing, within the experimental uncertainty, plasma measurements at various axial and radial locations, as well as

the keeper voltage. The keeper wear for the XIPS DHC is also re-produced within ~50% of the observed maximum. The XIPS DHC is the second cathode for which a variety of plasma measurements and the keeper erosion profiles have been closely re-produced thereby further reducing the risk associated with our understanding of this failure mechanism. Second, the work identifies the largest uncertainty in predicting keeper wear – the wave amplitude A – and illustrates that a change in the keeper material renders this uncertainty insignificant based on the life requirements of NASA science missions.

Acknowledgments

The research described in this paper was carried out by the Jet Propulsion Laboratory, California Institute of Technology, under a contract with the National Aeronautics and Space Administration. Reference herein to any specific commercial product, process, or service by trade name, trademark, manufacturer, or otherwise, does not constitute or imply its endorsement by the United States Government or the Jet Propulsion Laboratory, California Institute of Technology.

References

[1] Oh, D., and Goebel, D. M., "Performance Evaluation of an Expanded Range XIPS Ion Thruster System for NASA Science Missions," AIAA Paper 06-4466, July 2006.
[2] Hofer, R. R., Randolph, T. M., Oh, D. Y., Snyder, J. S., and de Grys, K. H., "Evaluation of a 4.5 kW Commercial Hall Thruster System for NASA Science Missions," AIAA Paper 06-4469, July 2006.
[3] Goebel, D.M., "Qualification of Commercial XIPS Ion Thrusters for NASA Deep Space Missions," AIAA Paper 08-4914, July 2008.
[4] Tighe, W., Chien, K., Solis, E., Rebello, P., Goebel, D., and Snyder, J., "Performance Evaluation of the XIPS 25-cm Thruster for Application to NASA Discovery Missions," AIAA Paper 06-4666, July 2006.
[5] Polk, J. E., and Tighe, W., "XIPS 25-cm Thruster Cathode Life Qualification for Use on Deep Space Missions," IEPC Paper 07-193, September 2007.
[6] Polk, J. E., "Ongoing Wear Test of a XIPS 25- cm Thruster Discharge Cathode," AIAA Paper 08-4913, July 2008.
[7] Mikellides, I. G., and Katz, I., "The Partially-Ionized Gas and Associated Wear in Electron Sources for Ion Propulsion, I: Neutralizer Hollow Cathode," *J. Prop. Power*, in press, 2008.
[8] Mikellides, I.G., Katz, I., Goebel, D.M., Jameson, K.K., and Polk, J.E., "The Partially-Ionized Gas and Associated Wear in Electron Sources for Ion Propulsion, II: Discharge Hollow Cathode," *J. Prop. Power*, in press, 2008.
[9] Tighe, W., Chien, K., Goebel, D., and Longo, R., "Hollow Cathode Ignition Studies at L-3 ETI," IEPC Paper 07-23, September 2007.
[10] Mikellides, I. G., Katz, I., Jameson, K. K., and Goebel, D. M., "Driving Processes in the Orifice and Near-Plume Regions of a Hollow Cathode," AIAA Paper 06-5151, July 2006.
[11] Private communication with D. M. Goebel
[12] Sagdeev, R. Z., and Galeev, A. A., *Nonlinear Plasma Theory*, Benjamin, New York, 1969, p. 103.
[13] Jameson, K. K., Goebel, D. M., and Watkins, R., "Hollow Cathode and Keeper-Region Plasma Measurements," AIAA Paper 05-3667, July 2005.
[14] Goebel, D. M., Jameson, K. K., Katz, I., and Mikellides, I. G., "Energetic Ion Production and Electrode Erosion in Hollow Cathode Discharges," *Phys. Plasmas*, Vol. 14, 103508 1-15 (online).
[15] Doerner, R. P., Whyte, D. G., Goebel, D. M., "Sputtering Yield Measurements During Low Energy Xenon Plasma Bombardment," *J. Appl. Phys.*, Vol. 93, No. 9, 2003, pp. 5816-5823.
[16] Doerner, R. P., "Low-Energy Sputtering Yields of Tungsten and Tantalum," *J. Vac. Sci. Technol. A*, Vol. 23, No. 6, 2005, pp. 1545-1547.
[17] Goebel, D. M., Jameson, K. K., Katz, I., and Mikellides, I. G., "Potential Fluctuations and Energetic Ion Production in Hollow Cathode Discharges," IEPC Paper 05-269, October 2005
[18] Domonkos, M. T., Foster, J. E., and Patterson, M. J., "Investigation of Keeper Erosion in the NSTAR Ion Thruster," IEPC Paper 01-308, Oct. 2001.
[19] Bell, E. W., Djuric, N., and Dunn, G. H., "Electron-Impact Ionization of In+ and Xe+," *Phys. Rev. A*, Vol. 48, No. 6, 1993, pp. 4286-4291.
[20] Miller, J. S., and Pullins, G. H., "Xenon charge exchange cross sections for electrostatic thruster models," *J. Appl. Phys.*, Vol. 91, No. 3, 2002, pp. 984-991.